energy&fuels

pubs.acs.org/EF

Article

Nanopore Evolution of the Upper Permian Organic-Rich Shales from Dalong Formation, Sichuan Basin, during Artificial Hydrous Pyrolysis

Waheed Hammouri, Xiaowen Guo,* Mahmoud Abbas, and Keqing Wang

Cite This: https://doi.org/10.1021/acs.energyfuels.3c00752

Read Online

ACCESS | Metrics & More | Article Recommendations

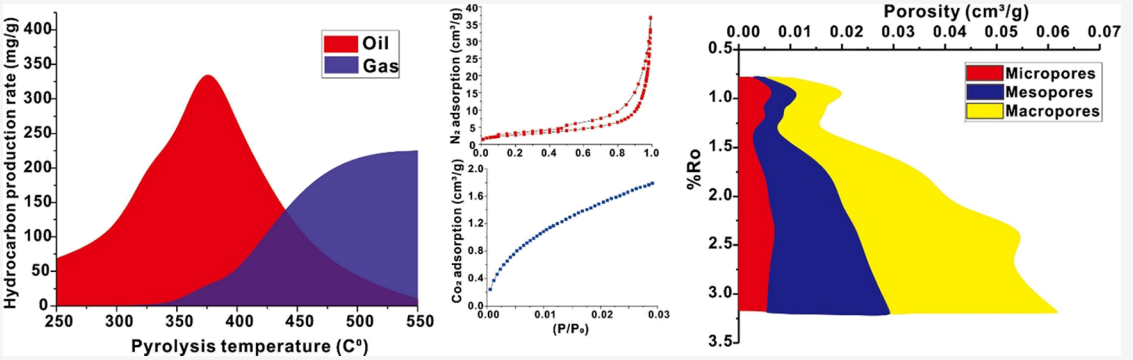

ABSTRACT: Shale pore evolution and variation are very important for evaluating shale reservoirs. In this study, hydrous pyrolysis experiments in a semiclosed system, low-pressure gas (N_2 and CO_2) adsorption, X-ray diffraction, organic petrography, and geochemistry experiments were applied on upper Permian organic-rich shale from Dalong Formation, Sichuan Basin, to understand the generation and evolution of nanometer-sized pores in shales. According to the pore structure parameters, most of the specific surface area (SSA) is supplied by micropores (<2 nm), whereas macropores (>50 nm) supply the bulk of the total pore volume (PV). The total PV and SSA are positively connected with thermal maturity (%R_o) and they share two peaks with corresponding %R_o values between 0.79−1.05% (peak I) and 1.83−2.35% (peak II), representing the two major periods of pore development. Peak I is associated with the late period of oil generation and the late period of kerogen cracking to gas, and peak II is associated with the cracking peak of the extractable organic matter (OM) to gas. The evolution of porosity was slightly affected by the mineral composition and total organic carbon (TOC) due to the main influence of thermal maturity, which masked the influence of mineral composition and TOC. Shale porosity formation and development are primarily influenced by diagenesis and hydrocarbon generation. Cementation can significantly reduce the overall porosity during diagenesis. It has been shown that OM pores are a function of thermal maturity, which is highly associated with the thermal cracking of both kerogen and secondary OM into hydrocarbon. During the overmaturity stage with %R_o > 2.67%, the porosity shows an increased trend due to the high gas generation rate. This illustrates that during the high maturity stage, OM pores are better formed, which is crucial for expanding shale gas exploration to more mature shale resources.

1. INTRODUCTION

Shale is an unconventional gas and oil reservoir with huge petroleum potential.[1−5] The pore structure is crucial for controlling gas storage and flow rates as well as evaluating shale gas resources.[6−9] The characteristics of pores, including their origin, morphology, quantity, structure, and distribution, along with the factors that control pore evolution, such as the content of total organic carbon (TOC), degree of thermal maturity, kerogen type, solid bitumen, and mineralogical compositions, play a significant role in the assessment of shale reservoirs.[6,10−19] Numerous studies have been carried out on shale pore structure and distribution using different techniques, i.e., direct imaging methods, small/ultrasmall-angle neutron scattering (SANS/USANS), gas adsorption methods, mercury intrusion analysis, atomic force microscopy (AFM), scanning electron microscopy (SEM), as well as nuclear magnetic resonance (NMR).[8,20−25] Porosity development in shales is influenced by various factors, but the degree of kerogen maturation and secondary cracking of crude oil and/or bitumen to gas are crucial.[26] Therefore, it is necessary to investigate the formation and development of nanopores in organic-rich shales

Received: March 7, 2023
Revised: April 19, 2023

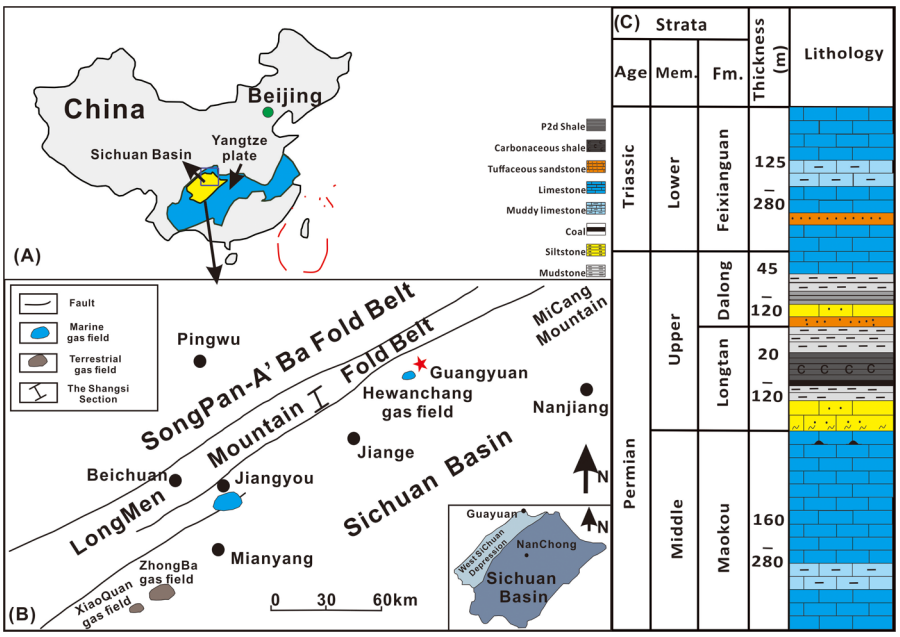

Figure 1. Geographical map of the current work. (A) Geographical location; (B) research region displaying the location of the sample; and (C) lithological column of the research region.

during the hydrocarbon generation process. Hydrous pyrolysis is the basic step to maturate and extract the hydrocarbons of shale, and it has been shown to simulate natural petroleum formation.[27,28] Systems of pyrolysis experiments can be divided into closed, open, and semiclosed parts, which will produce different results of hydrocarbon generation and pore evolution of shales.[29] A semiclosed system, such as the experimental one applied in this study, is closer to natural conditions, especially the axial pressure of the apparatus, which can simulate the real situation of organic matter (OM) evolution in geological burial processes.[29]

Pyrolysis experiments on organic-rich shales revealed that the abundance of OM pores varies depending on the stage of thermal maturity (%R_o), which increases with increasing %R_o, as a result of gas expulsion throughout the conversion of OM.[14,17,26,30−32] Feiyu et al.[33] showed that the formation of organic pores would occur at 1.3−2.0%R_o, while when %R_o is greater than 2.0%, organic pores tend to diminish. However, Fishman et al.[34] claimed that the hydrocarbon generation processes are not connected to the preserved OM pores in shales, because it appears that the OM pores formed through the hydrocarbon generation were not preserved owing to the extremely flexible character of OMs and other components of shale. Experimental outcomes of porosity evolution of the immature shale pyrolyzed are still a debated issue. Hydrous pyrolysis tests were carried out by Tang et al.[35] on samples collected from the lacustrine shale of the Ordos Basin, Late Triassic Chang_7, in Northwest China and found that the number of micropores and mesopores grow as the pyrolysis temperature increases, whereas macropores remain unchanged at the overmature stage. Wu et al.[36] concluded that the highest porosity of Chang_7 shale occurs with a %R_o value between 2.5 and 3.0%, while Liu et al.[37] proposed that the porosity of shale decreases slowly when thermal maturity is in the overmature phase. Limited studies have been conducted on the evolution of porosity using CO_2 adsorption analysis. Cao et al.[25] employed the N_2 adsorption method to investigate the evolution of nanopores during thermal maturation on Dalong shale. However, N_2 adsorption cannot evaluate pores smaller than 1 nm in diameter, which is insufficient to examine the micropores. In this study, N_2 adsorption as well as CO_2 adsorption, which is more precise for examining the micropores, has been employed to investigate the development of porosity and its relationship with evolution in minerals during pyrolysis.

So far, the factors controlling porosity development in shale resources are still controversial. Although numerous studies have examined the influence of thermal maturity on pore development utilizing naturally occurring shale samples or samples that have been artificially matured, most of the viewpoints are not consistent, e.g.,[25,33,36,37] nano-scale pore structure creation and evolution mechanisms upon increasing thermal maturation still need to be investigated.

In this research, the marine organic-rich shale samples containing type II_1 kerogen were collected from the Late Permian Dalong Formation, Northern Sichuan Basin, China, and pyrolyzed in a semiclosed unit system. Gas adsorption, organic petrography, and mineralogy analysis were performed to identify the parameters influencing pore development in organic-rich shales. The mechanisms of pore structure evolution and porosity formation were studied. The outcomes can provide important insights into the comprehensive understanding of the processes of formation and evolution of nanopores of organic-rich shale during hydrous pyrolysis.

2. SAMPLES AND METHODS

2.1. Samples and Geological Setting. To better understand the mechanisms underlying the formation and development of marine shale pores during the petroleum production process, immature marine organic-rich shales were collected from the Shangsi part in the Guangyuan region of the Late Permian Dalong Formation (P2d), in the northwest portion of the Sichuan Basin (Figure 1A,B). The Sichuan Basin is situated on the South China plate, particularly on the upper Yangtze region (Figure 1), and it has deposited in a collection of comparatively full stratigraphic sequences between the period of Neoproterozoic to the Neogene, with a total thickness of 6−12 km.[38,39] The Dalong Formation comprises black siliceous shale, gray-black shale, limestone, and silty shale (Figure 1C).

https://doi.org/10.1021/acs.energyfuels.3c00752
Energy Fuels XXXX, XXX, XXX−XXX

Table 1. Hydrocarbon Production Rate of the Semiclosed Pyrolysis Experiment for P2d Organic-Rich Shale with Various Thermal Simulation Temperatures

thermal simulation temperature (°C)	strata pressure (MPa)	lithostatic pressure (MPa)	R_o, %	total gas (mL/g)	CO_2 (mL/g)	H_2 (mL/g)	hydrocarbon gas (mL/g)	hydrocarbon gas (mg/g)	residual oil (mg/g)	expulsed oil (mg/g)	light residual oil (mg/g)	total oil (mg/g)	chloroform bitumen "A" (mg/g)	total hydrocarbon (mg/g)
250	37.5	58	0.69	18.20	2.25	0.28	0.21	0.18	66.24	1.82	1.33	68.06	64.91	68.25
300	57.5	68	0.75	5.75	1.16	0.42	0.68	0.63	100.95	1.84	4.08	102.79	96.88	103.42
325	57.5	74	0.84	3.79	0.90	0.42	1.47	1.53	200.48	6.58	19.16	207.06	181.32	208.59
350	75	80.5	1.15	9.39	3.04	0.87	4.64	5.24	235.64	5.75	27.57	241.39	208.07	246.63
375	80	86.2	1.38	42.33	9.14	0.31	29.79	33.19	284.56	92.00	22.25	376.56	262.31	409.76
400	84	92	1.56	51.74	10.92	0.20	36.55	41.21	187.27	71.18	12.95	258.44	174.32	299.65
450	92	103	1.87	193.86	35.46	0.97	154.73	171.33	36.11	62.26	10.15	98.37	25.96	269.70
500	100	112	2.56	310.84	49.82	2.15	255.34	221.92	3.55	34.32	2.23	37.88	1.32	259.79
550	105	115	3.45	495.25	110.64	7.72	296.21	225.24	1.57	8.38	0.51	9.94	1.06	235.18

The P2d shales ranged in thickness from 10 to 60 m and were predominantly developed in the narrow basin between Guangyuan-Wangcang and Liangping in the Sichuan basin (Figure 1B).[32,40] Organic-rich shales in the Dalong Formation were deposited in deep-water under an anoxic sedimentary environment with TOC values varying from 0.3 to 12%.[38,40−42] The OM is mostly Type II_1 and $\delta^{13}C_{org}$ values range from −28.5 to −25.2‰.[40,42]

2.2. Methods. One block sample of P2d organic-rich shale was collected and divided into 12 core samples and nine powder samples. The 12 core samples were used for the hydrous pyrolysis experiment, and the original and artificial pyrolysis samples were crushed for the geochemical and low-pressure gas adsorption analysis in order to investigate the pore evolution. The nine powder samples were pyrolyzed to determine the hydrocarbon production rate.

2.2.1. Hydrocarbon Pyrolysis Experiment. The hydrocarbon generation hydrous pyrolysis experiment under a semiclosed system was carried out on an ejection thermal simulation device.[43] The device can simulate the hydrocarbon generation and expulsion under high temperatures and high fluid pressure with formation water. The instrument contains two major sections: the software system, which is utilized to enter the experimental settings and data collection, along with the hardware operating system. Approximately 40−60 g of core samples were placed within a cylinder made of stainless steel (34 mm i.d.). Every cylindrical sample was inserted into an autoclave and subjected to the designated conditions for the simulation experiment. Shale samples were placed between the plunger cores and an autoclave, and a copper ring with good heat resistance was used to seal the autoclave. The hydrocarbon generation system was performed with a leakage test in advance before the hydrous pyrolysis experiment of each temperature point. After making sure no leaks are present, the system was vacuumed, and formation water was pumped into an autoclave.

Finally, the samples were heated to complete the process. The temperatures used in this study for hydrous pyrolysis were 250, 275, 300, 325, 350, 375, 400, 425, 450, 475, and 500 °C. In order to reach the desired temperature, a thermostatic furnace was heated at a rate of 5 °C/min. At each temperature point, the instrument was maintained for 48 hto guarantee complete pyrolysis for hydrocarbon production and pore evolution. The hydrostatic pressure was initially set to 25 MPa, with less than 1 MPa of deviance. The entire experimental process is a semiclosed system. The device can expel hydrocarbons automatically when its internal pressure rises above the preset pressure. After completing each pyrolysis experiment, the expelled oil and water were collected. The solid residues were collected after the autoclave cooled naturally. The samples have been divided into different portions to apply other experiments such as X-ray diffraction (XRD) analysis, R_o measurement, TOC analysis, and low-pressure gas adsorption analysis.

The same pyrolysis experiment was conducted for hydrocarbon generation. One origin core sample with a TOC content of 12.38% was crushed to powder and then divided into nine parts (40−60 g). The samples were pyrolyzed under a semiclosed system at temperatures of 250, 300, 325, 350, 375, 400, 450, 500, and 550 °C, with different pressures, as shown in Table 1. Oil, gas, and residual products were gathered after completing each pyrolysis experiment, and measurements were made of the amount and composition of oil and gas. An Agilent 6890N gas chromatograph (GC) device was used to measure C_{1-5} hydrocarbons and C_{6-14} hydrocarbons. C_{14+} hydrocarbons were extracted by dichloromethane (CH_2Cl_2) and then the quantity of gas hydrocarbon (C_{1-5}) and liquid hydrocarbon (C_{6-14}, C_{14+}) were determined.

2.2.2. TOC, %R_o, and Mineralogy. The TOC contents were analyzed by a rapid CS cube carbon and sulfur analyzer.[41] A TOC test was conducted on powdered shale samples between 10 and 100 mg. Soxhlet extraction was carried out with a combination of acetone, trichloromethane, and methanol (0.38:0.32:0.30 vol/vol/vol) for 48 h, in order to clean the samples from carbonate residues produced from pyrolysis. The powder samples were treated with a diluted solution of hydrochloric acid with a volume ratio of 1:7 to eliminate the inorganic carbon from the shale samples. After being cleaned of the remaining HCl with distilled water for roughly 24 h, the samples were dried. The samples were placed in an oxygen flow at a high temperature (930 °C)

https://doi.org/10.1021/acs.energyfuels.3c00752
Energy Fuels XXXX, XXX, XXX−XXX

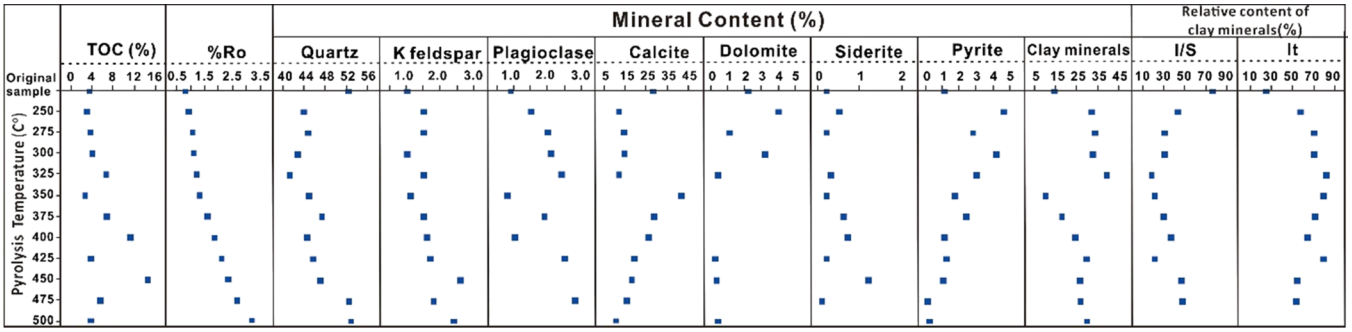

Figure 2. Geochemical characteristics of organic compounds and mineral compositions of the P2d organic-rich shales with different thermal simulation temperatures.

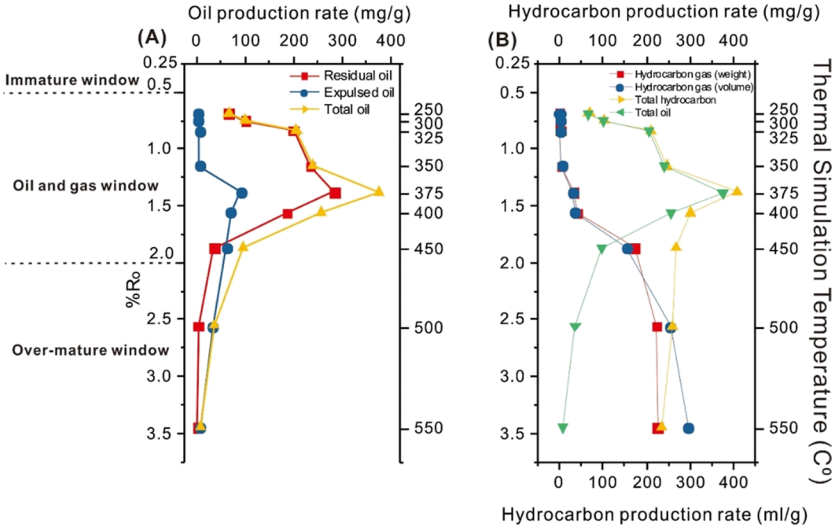

Figure 3. Hydrocarbon generation with increased thermal maturity (%R_o) at different thermal simulation temperatures for P2d organic-rich shale. (A) Rate of oil generation and (B) rate of oil and gas generation. The maximum hydrocarbon generation rate is about 409.76 mg/g at 375 °C for 1.38% R_o.

to burn, and the TOC content is calculated according to the CO_2 content, which was measured by a CO_2 infrared detector.

Vitrinite reflectance (VR) under oil immersion was examined by a German Leica DM IL LED microscope to determine the thermal maturity (%R_o) of the pyrolyzed samples. Two standard samples with %R_o < 0.5% and %R_o > 3.5% were used to calibrate the microscope. Twenty measurements on vitrinite particles were averaged to get the VR values for every single sample at a temperature of around 23 °C with a relative humidity of lower than 70%.[31]

The mineral composition was quantitatively determined using XRD analysis.[44] Core samples were mashed to fine-grained powders and placed on a flattened glass plate with grooves. The powder samples were then scanned from 5° to 80° (2θ) with a scanning velocity of 2°/min. Finally, diffraction peak intensity was used to calculate the relative content of mineral compositions.

2.2.3. Low-Pressure CO_2 and N_2 Gas Adsorption. An Autosorb-IQ3 specific surface area (SSA) and pore size analyzer was utilized to analyze the pyrolyzed and original core samples in low-pressure and low-temperature N_2 and CO_2 gas sorption in order to quantitatively evaluate porosity development in marine organic-rich shale with increasing thermal maturity. Core samples were broken down into particles ranging in size from 60 to 80 meshes. To eliminate volatile substances and moisture, the particle samples were vacuum-dried and degassed at 105 °C for 8 h. N_2 adsorption experiments were carried out in order to investigate the properties of mesopores and macropores. N_2 adsorption and desorption isotherms were conducted under the following conditions; a temperature of −195.6 °C (77.3 K) coupled with a relative pressure (P/P_0) range of 0.001−0.998 (saturated vapor pressure of N_2).[45] Analysis of N_2 sorption yields information on pores with a diameter of 1.7−350 nm. The SSA and average pore diameter were assessed utilizing the model of Brunauer−Emmett−Teller (BET), whereas pore volume (PV), SSA, as well as pore size distribution (PSD) of mesopores and macropores were assessed by the Barrett−Joyner−Halenda (BJH) model.[46,47] The fractal dimension was determined by the Frenkel−Halsey−Hill (FHH) model.[48] The micropore (<2 nm) measurements were carried out using a low-temperature CO_2 adsorption experiment. CO_2 sorption isotherms were carried out with relative pressures (P/P_0) ranging from 0.00 to 0.03 at 0 °C, which can provide data of pores with a diameter of 0.3−1.5 nm. The density functional theory (DFT) was used to determine the PV, SSA, and PSD of micropores.[21]

3. RESULTS

3.1. Organic Geochemistry and Mineralogy. The TOC content and mineral compositions of the original and simulated samples are shown in Figure 2. The original P2d organic-rich shale sample has a TOC content of 3.3% and a %R_o value of 0.79% (Figure 2). The original sample is primarily composed of quartz (52.2%), calcite (28.2%), and clay minerals (14%). The clay minerals primarily contain an illite and illite/smectite mixed layer. Minor amounts of dolomite (2.2%), pyrite (1.1%), and K-feldspar (1%) are present, whereas the plagioclase and siderite contents are less than 1.1%. The TOC concentration fluctuates with different simulated temperatures because the OM in shale is heterogeneous (Figure 2). The values of %R_o increase with increased pyrolysis temperature. The simulated samples show variations in mineral composition with different pyrolysis temperatures. The content of clay minerals and calcite dropped

https://doi.org/10.1021/acs.energyfuels.3c00752
Energy Fuels XXXX, XXX, XXX−XXX

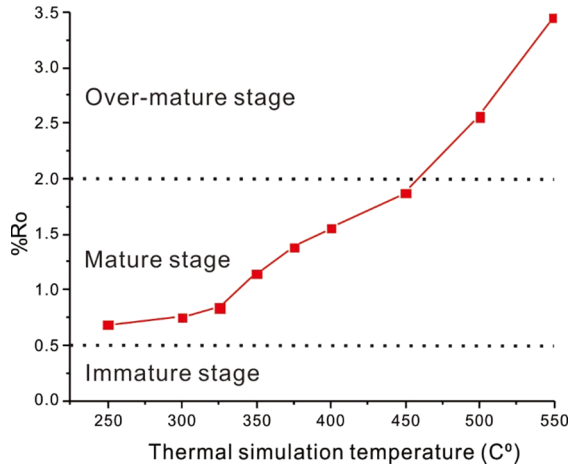

Figure 4. Appropriate relation between thermal simulation temperature and $\%R_o$ values of P2d organic-rich shales during the whole semiclosed pyrolysis experiment, showing that $\%R_o$ is strongly correlated with temperature.

to a certain amount, indicative of participation in the hydrocarbon production operations.[49] The amount of illite/smectite mixed layers dropped and the amount of illite increased with increasing thermal maturity.

3.2. Hydrocarbon Generation. Table 1 and Figure 3 show the analyzed results of hydrocarbon generation products with the increased simulated temperature of the P2d organic-rich shale. In the beginning, the hydrocarbon generation rates of crude oil and residual oil show an increasing trend and then drop down with the simulated temperature increase. The rate of oil production shows a rapid raise at a $\%R_o$ of 0.69% with a simulated temperature of 250 °C (Figure 3A). The maximum oil generation rate is about 376.56 mg/g at a temperature of 375 °C corresponding to a $\%R_o$ of 1.38%. After going through the oil window, the generation rate of expulsed oil gradually increased with increasing thermal maturity. The maximum rate of oil expulsion occurred at a $\%R_o$ of 1.38%, with a value of around 92 mg/g, and after this decreased slightly until a $\%R_o$ of 3.45% (Figure 3A).

The varying trend of the residual oil production rate is similar to that of the overall oil. While $\%R_o$ is about 1.38%, the residual oil generation arrived at a peak value of 284.56 mg/g at a temperature of 375 °C and then decreased with increasing thermal maturity. The generation rate drops slightly and then keeps almost constant when the $\%R_o$ exceeds 2.5%. The measured $\%R_o$ values at each simulated stage are strongly correlated with the simulated temperature (Figure 4).

During the whole hydrocarbon generation process, the rate of total hydrocarbon and gas generation increases with increasing $\%R_o$ values and pyrolysis temperatures (Figure 3B). The high gas generation rate stage occurs at $\%R_o$ > 1.56%. The main oil generation stage occurs at the oil and gas window when the maturity is between 0.5 and 2%. Gas generation during the oil window is minor and is mostly generated by the cracking of kerogen. The gas generation content increases while the liquid hydrocarbon content decreases when $\%R_o$ values exceed 1.56%. The major stage of cracking crude oil into gas occurs when $\%R_o$ is between 1.56 and 3.45%. The maximum hydrocarbon gas production rate is 225.24 mg/g with a $\%R_o$ value of 3.45% (Figure 3B).

3.3. N_2 Adsorption. N_2 sorption isotherms of original samples and simulated samples belong to type IV according to the classification of physisorption isotherms (IUPAC), whereas the hysteresis loops belong to type H3 (Figure 5). The appearance of hysteresis loops is a sign that mesopores and macropores are present.[50,51] Adsorption capacity has a positive relationship with relative pressure. The N_2 adsorption capacity grows with the increasing P/P_0 (Figure 5). The maximal N_2 adsorption volumes exhibit a positive relationship with increased simulated temperatures. When the relative pressure exceeds 0.40, the capillary condensation causes the adsorption−desorption isotherms to split, creating a hysteresis loop. The hysteresis loop shapes are largely controlled by pore shapes, such as plate or wedge-formed, slit formed pores, and ink bottle pores.[52] Based on the patterns of the hysteresis loops, the investigated shales include assemblages of flexible platelike particles (such as clays) and the macropores are not filled with pore condensates.[53]

The BET surface area of the original and simulated shale samples varies from 0.923 to 9.850 m^2/g with an average value of 4.45 m^2/g (Table 2). Mesopores and macropores have a surface area that varies from 0.9390−7.3800 to 0.1400−1.1500 m^2/g, respectively. The PSD versus incremental PV and surface area of both original and simulated samples are illustrated in Figure 6. The macropores were rarely developed during pyrolysis from the original sample to 350 °C. For pore size <10 nm, the pores were strongly developed during pyrolysis (Figure 6).

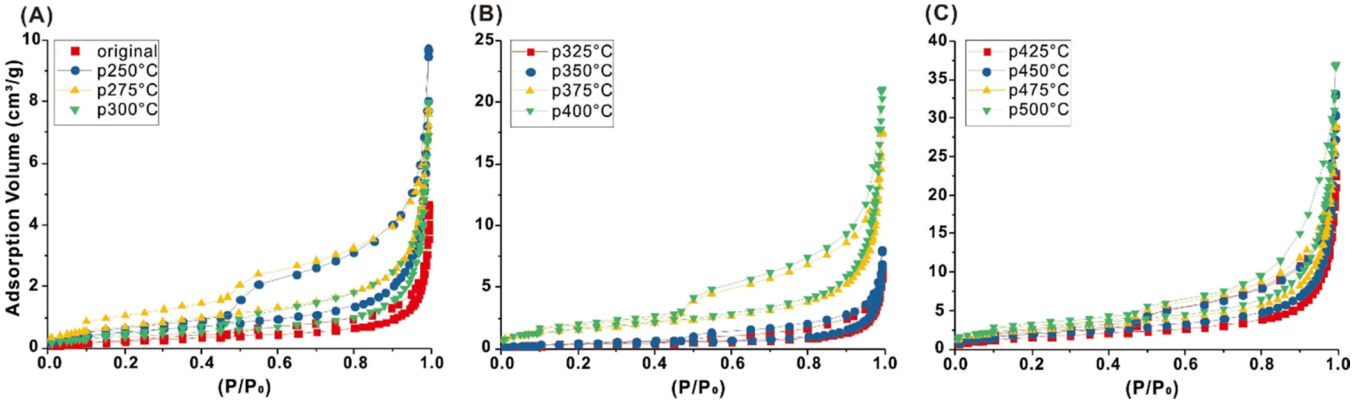

Figure 5. N_2 adsorption and desorption isotherms of P2d organic-rich shale at different thermal simulation temperatures (A) 0−300 °C, (B) 325−400 °C, and (C) 425−500 °C, which belong to type IV based on the categorization of physisorption isotherms (IUPAC), and the hysteresis loops belong to type H3. In this graph, the equivalent desorption curve is above the adsorption curve.

https://doi.org/10.1021/acs.energyfuels.3c00752
Energy Fuels XXXX, XXX, XXX−XXX

Table 2. PVs and Surface Areas of Micropores, Mesopores, and Macropores Computed Using N_2 and CO_2 Gas Adsorption Isotherms at Different Thermally Simulated Temperatures

sample ID	fractal dimension	average pore diameter (nm)	CO_2 adsorption		N_2 adsorption				BET SSA (m^2/g)	total PV (cm^3/g)	total SSA (m^2/g)	percent of PV (%)			percent of SSA (%)		
			PV micro (cm^3/g)	SSA micro (m^2/g)	PV meso (cm^3/g)	SSA meso (m^2/g)	PV macro (cm^3/g)	SSA macro (m^2/g)		micro + meso + macro	micro + meso + macro	micropore	mesopore	macropore	micropore	mesopore	macropore
P original	2.4868	31.1575	0.0031	8.8200	0.0024	0.9390	0.0049	0.1400	0.9230		9.8990	30.0672	22.6705	47.2622	89.0999	9.4858	1.4143
P250	2.5086	30.2313	0.0074	22.8660	0.0049	1.7300	0.0102	0.3210	2.0460	0.0225	24.9170	32.9035	21.7430	45.3535	91.7687	6.9431	1.2883
P275	2.5898	17.6332	0.0049	15.0340	0.0054	2.4400	0.0066	0.2240	2.7010	0.0169	17.6980	29.0112	31.9716	39.0172	84.9475	13.7869	1.2657
P300	2.4466	34.3493	0.0046	13.7930	0.0038	1.2000	0.0085	0.2720	1.4920	0.0169	15.2650	27.1707	22.6226	50.2067	90.3570	7.8611	1.7819
P325	2.4272	32.0219	0.0057	16.9370	0.0034	1.0300	0.0069	0.2260	1.2840	0.0160	18.1930	35.6696	21.2140	43.1164	93.0962	5.6615	1.2422
P350	2.4431	34.2831	0.0020	6.0802	0.0038	1.1700	0.0086	0.2750	1.4460	0.0144	7.5252	13.8889	26.3889	59.7222	80.7979	15.5478	3.6544
P375	2.5593	19.2175	0.0034	10.5890	0.0111	4.5300	0.0158	0.5550	5.7100	0.0303	15.6740	11.2211	36.6337	52.1452	67.5577	28.9014	3.5409
P400	2.5252	21.5353	0.0056	18.3950	0.0131	4.8900	0.0192	0.6980	6.118	0.0379	23.9830	14.7757	34.5646	50.6596	76.7002	20.3894	2.9104
P425	2.4942	24.9462	0.0058	18.6450	0.0141	4.6500	0.0209	0.7370	5.667	0.0408	24.0320	14.2157	34.5588	51.2255	77.5841	19.3492	3.0667
P450	2.4691	28.7844	0.0075	27.8840	0.0157	5.3800	0.0352	1.1500	7.125	0.0584	34.4140	12.8425	26.8836	60.2740	81.0252	15.6332	3.3417
P475	2.5352	19.8656	0.0059	21.6920	0.0188	6.6000	0.0253	0.9150	9.0330	0.0500	29.2070	11.8000	37.6000	50.6000	74.2699	22.5973	3.1328
P500	2.5038	23.1853	0.0054	18.3580	0.0240	7.3800	0.0324	1.1400	9.8490	0.0618	26.8780	8.7379	38.8350	52.4272	68.3012	27.4574	4.2414

The volumes of mesopores and macropores vary from 0.0024−0.240 to 0.0049−0.0352 cm^3/g, respectively. PV and surface area exhibit a negative relation with the pore diameter. The PV and surface area decrease with the increasing pore diameter, indicating that large-sized pores have a low PV and surface area. Multiple peaks could be seen on the PSD curves (Figure 6A−C). PV fluctuates considerably with pore size in the range of 2−10 nm, indicating that mesopores are mostly spread among this range and are more than macropores. Noteworthy is the fact that both the original and pyrolyzed samples display multiple peaks in the 50−100 nm pore diameter region, indicating that the macropore volume in this range is developed.

3.4. CO_2 Adsorption. Following the IUPAC classification, the low-pressure CO_2 adsorption isotherms can be categorized as type I. The original sample has less adsorbed CO_2 amounts than that of the pyrolyzed samples with pyrolysis temperature >350 °C, indicating that micropores were created abundantly during pyrolysis. At relative pressures (P/P_0) of 0.0290, the maximum CO_2 adsorption volume varies from 0.6182 to 2.8401 cm^3/g (Figure 7). The maximum CO_2 adsorption amount increases from the original sample to 250 °C and then the values decrease to the minimum point at 350 °C. After this, the CO_2 adsorption amount increases from 350 to 450 °C, and finally, the quantities decline at 475−500 °C. The CO_2 adsorption capacities of simulated samples exhibit a minimal value during the peak oil generation and are higher than the original sample as soon as the pyrolysis temperature is >350 °C.

The original sample has a surface area of 8.82 m^2/g and a pore volume of 0.0031 cm^3/g. The PV and surface area vary at different thermal maturity stages. The micropore volume varies from 0.002 to 0.0075 cm^3/g with an average value of 0.0051 cm^3/g, whereas the surface area of the micropore varies from 6.08 to 27.88 m^2/g with an average value of 16.59 m^2/g, where the maximum value was at a pyrolysis temperature of 450 °C (Table 2).

The PSD of micropores with a range from 0.3 to 1.5 nm is depicted in Figure 8. All the PSD curves, including both PV and surface area, have a triple-peak feature, correlating to pore diameters of 0.3−0.4, 0.45−0.65, and 0.82 nm, indicating that the surface area and PV of micropores are mostly distributed in these three segments (Figure 8). At a pore diameter of 0.34 nm and a temperature of 450 °C, the highest values of $dV(d)$ and $dS(d)$ are recorded (Figure 8), suggesting that the volume and surface area of pores are significantly increased by pores with relatively small sizes.

4. DISCUSSION

4.1. Pore Development with Increasing Thermal Maturity. The pyrolysis of organic-rich shale is quite complicated because several reactive processes concurrently occur, including devolatilization, dehydration, and structural regulation, leading to the generation of various organic and inorganic compositions and nanometer-scale pores.[54] Pore structures of P2d organic-rich shale with increasing thermal maturity are displayed in Figure 9. The PV is mainly provided by macropores yielding a percentage of 39−67.5% with an average value of 51.5%, mesopores yielding 21.2−40.6% with an average value of 28.7%, and micropores yielding 10.6−35.6% with an average value of 19.6% (Figure 9A,B). The SSA is mainly provided by micropores accounting for 67.5−93% with an average value of 80.9%, followed by mesopores yielding 5.6−28.9% with an average value of 16.2%, and macropores with a

https://doi.org/10.1021/acs.energyfuels.3c00752
Energy Fuels XXXX, XXX, XXX−XXX

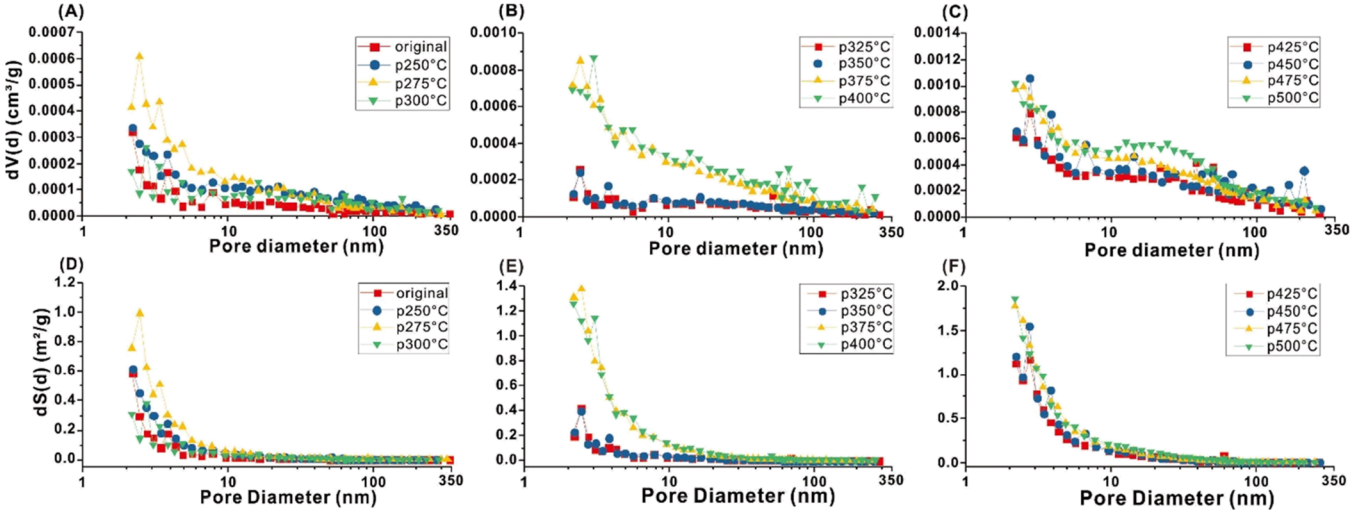

Figure 6. PSD versus incremental PV (A−C) and surface area (D−F) at different thermally simulated temperatures. The PSD curves show a multipeak characteristic with a diameter in the range of 2−10 and 50−100 nm, indicating that pores are mainly distributed in this range.

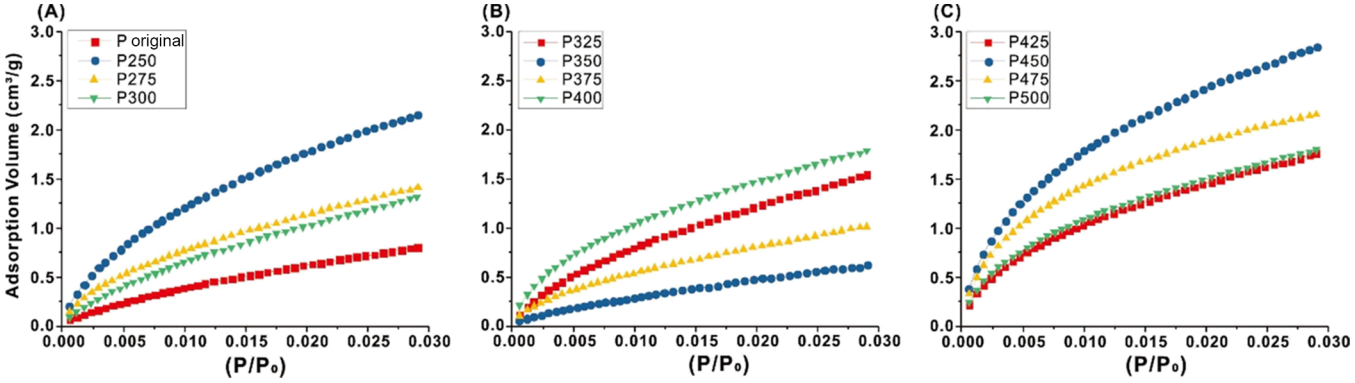

Figure 7. CO_2 adsorption isotherms of P2d organic-rich shales at various thermally simulated temperatures (A) 0−300 °C, (B) 325-400 °C, and (C) 425−500 °C, which are categorized as type I following the IUPAC classification.

minor contribution between 1.2 and 4.4% with an average value of 2.7% (Figure 9C,D).

The PV and SSA were associated with thermal maturity to describe the evolution of pore structure with increasing thermal maturity (Figure 10). The total PV and SSA increase with increasing thermal maturity. The increasing thermal maturity also causes both the micropore surface area and mesopore volume to rise. However, the PV and SSA have low values at a thermal maturity $\%R_o$ of 1.32% (Figure 10A,B). With increasing thermal maturity, there is no discernible change in the macropore surface area or micropore volume. The macropore volume has two low-value points at a $\%R_o$ of 1.32 and 2.67%. The variations in the total PV and macropore volume are similar, showing an increasing trend when $\%R_o$ > 1.32%. The total surface area has a similar trend to that of the micropore surface area, displaying an increasing trend when $\%R_o$ exceeds 1.32% (Figure 10). Two peaks can be seen in the PV and SSA with $\%R_o$ values of 0.92 and 2.35%. Peak I is lower than peak II. The drop of PV macro and total PV at the stage of $\%R_o$ less than 1.3% was likely caused by oil filling, which reduced inorganic pores.[15,55] The growth of the macropore volume and total PV with a maturity >1.3% was possibly connected to mineral dissolution by organic acids and organic pore development as a result of the cracking of oil.[15,56] This is also confirmed that numerous organic pores can develop during the thermal cracking of kerogen and liquid hydrocarbon to gas.[18,57] In general, marine shale is known to exhibit a more pronounced pore structure compared to transitional shale,[58] and this phenomenon is also observed in the current study. The comparison of the pore structure and fractal dimension between the marine P2d organic-rich shale from Sichuan Basin and the transitional shale from the east margin of the Ordos Basin, China, at the same level of maturity, shows that P2d organic-rich shale has higher PV and surface area.[59] Both marine shale and transitional shale have fractal dimensions greater than 2 with little increase for transitional shale, indicating that their pore surfaces are complex and irregular.[48] The increased PV and surface area in marine shale can be attributed to the presence of higher OM pores.[60] Consequently, the gas capacity of marine shale is generally higher than that of lacustrine and transitional shale.

4.2. Factors Controlling Nanopore Evolution. Previous research studies demonstrated that the TOC content significantly affects the evolution of nanopores as a result of the transformation of the OM to gaseous and liquid hydrocarbons.[13,21,61,62] Porosity increases with increasing TOC content.[15,63,64] Figure 11 displays the relationship between TOC and PV and surface area for both the original and pyrolyzed samples. TOC contents have no relationship with pyrolysis temperature with $\%R_o$ increasing from 0.69 to 3.18%, demonstrating that the formation of nanopores is not primarily

https://doi.org/10.1021/acs.energyfuels.3c00752
Energy Fuels XXXX, XXX, XXX−XXX

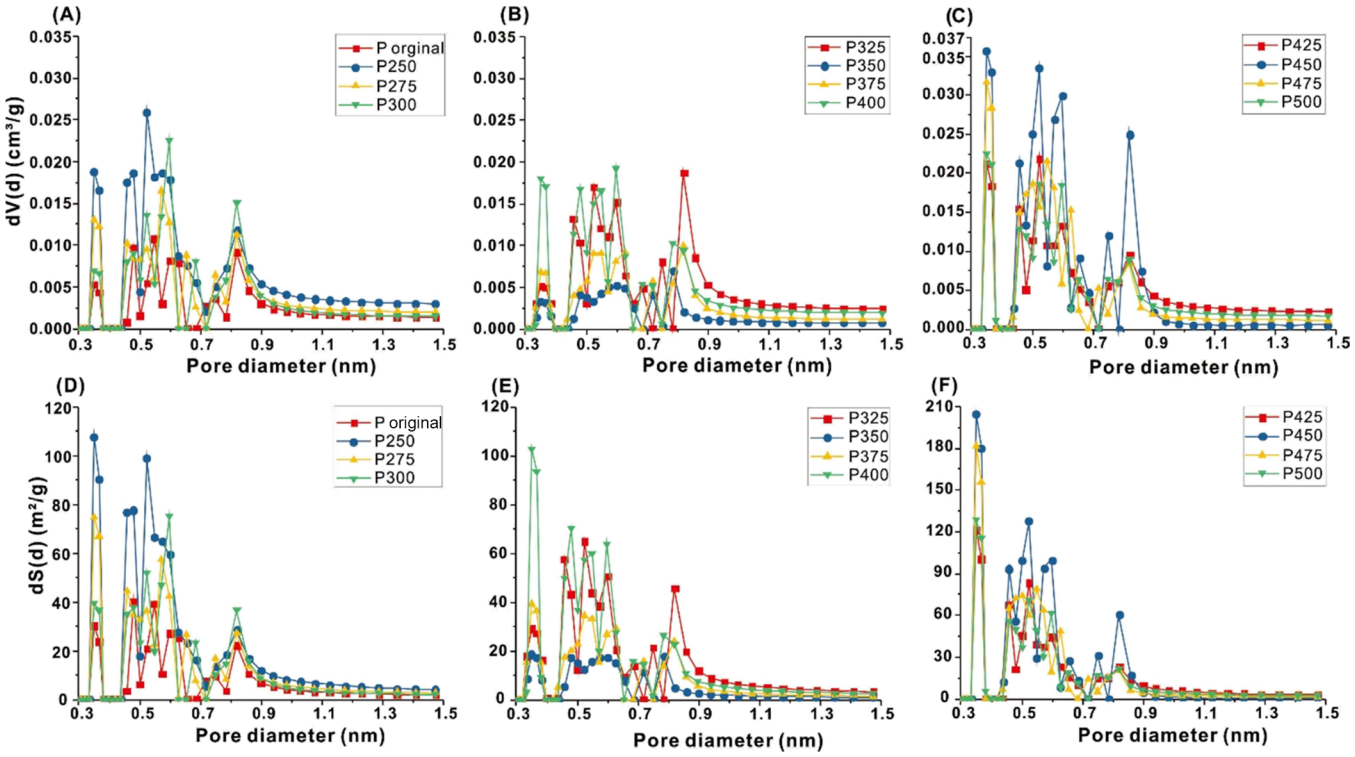

Figure 8. Micropore size distribution of PV (A−C) and surface area (D−F) for P2d organic-rich shale at various thermal simulation temperatures. The PSD curves include a tribal-peak feature, corresponding to pore diameters of 0.3−0.4, 0.45−0.65, and 0.82 nm, which show that micropores are mainly distributed in these ranges.

influenced by the TOC content. The difference in TOC contents could be attributed to the shale rock heterogeneity.[25,65] For instance, the TOC content of the original sample is 3.34%, whereas the pyrolyzed samples have a TOC content range from 2.55 to 14.47% (Figure 2). For P2d organic-rich shale, there is no clear relationship between TOC, SSA, and PV (Figure 11), which is probably due to the strong influence of thermal maturity. The thermal maturation of the OM results in the formation of a significant number of micropores, and this could substantially influence the SSA and PV.[26,66,67] P2d organic-rich shale could not be described by OM alone due to these weak correlations of TOC with SSA and PV. High-mature shale samples typically have high porosity.[22,68] Our result implies that shale porosity significantly increases with increased thermal maturity. The TOC content is a second important factor to control the organic porosity evolution during hydrous pyrolysis because a significant amount of OM pores were produced during pyrolysis.[50,69−71] The lately created pores in P2d organic-rich shale were generated mostly by the thermal cracking of OM during the simulation procedure.

Mineralogical composition is a potential factor affecting nanopore evolution with increased thermal maturity.[12,13,17,18,26,72,73] The mineral compositions of P2d organic-rich shale are depicted in Figure 2, and the predominant minerals are quartz, calcite, and clay. Figure 12 depicts the evolution of minerals and the properties of the pore structure during the pyrolysis process. Clay minerals and calcite only had a relationship with micropores, while the other pore structure parameters did not show a clear relationship with these minerals during hydrous pyrolysis. Clay minerals and OM are favorable for gas adsorption. The nature and content of clay minerals varied with diagenesis leading to different pore structures and capacities of adsorption.[74] The degree of conversion of clay minerals is influenced by the maturity of the shale, and the transformation progresses as maturity levels rise.[74] During the pyrolysis process, the content of illite−smectite mixed layers gradually decreases, and the content of illite increases (Figure 2). Clay minerals and the micropore volume and surface area are positively correlated with maturity $\%R_o$ < 1.59%, and at this stage of maturity, illite/smectite pores increase gradually in size with increasing temperature. Originals are connected by newborn fractures and the connectivity of the whole system improves (Figure 12A,E). However, no obvious relationship is observed when the maturity is higher than 1.59% (Figure 12A,E) demonstrating that clay mineral evolution may take place in the maturity stage of $\%R_o$ < 1.59% and contribute to increase the porosity.[75] With increasing maturity, the diagenesis degree of clay minerals increases. Diagenesis of clay minerals mainly includes the dehydration and microstructural change resulting in an obvious decrease of the porosity, as well as the transformation of the mineral type (typically smectite to illite through a mixed-layer illite−smectite). As catagenesis changes to metagenesis, illite crystallinity increases, resulting in the development of hydromicas and mica and a decreased contribution to porosity.[76,77] Both the micropore volume and the surface area have a negative association with calcite (Figure 12A,E). The negative associations of calcite with porosity could be from the thermal maturity impact. The organic acid-generated association with the hydrocarbon generation could cause several brittle minerals, including feldspar and calcites, to dissolve, causing the calcite concentration to drop and the formation of new pores.[78]

4.3. Effect of Thermal Maturity on Pore Evolution. P2d organic-rich shales with high OM and high $\%R_o$ typically have high surface areas and pores volumes, exhibiting a slightly positive connection with TOC contents (Figure 11). TOC content has a certain impact on pore evolution, whereas the

https://doi.org/10.1021/acs.energyfuels.3c00752
Energy Fuels XXXX, XXX, XXX−XXX

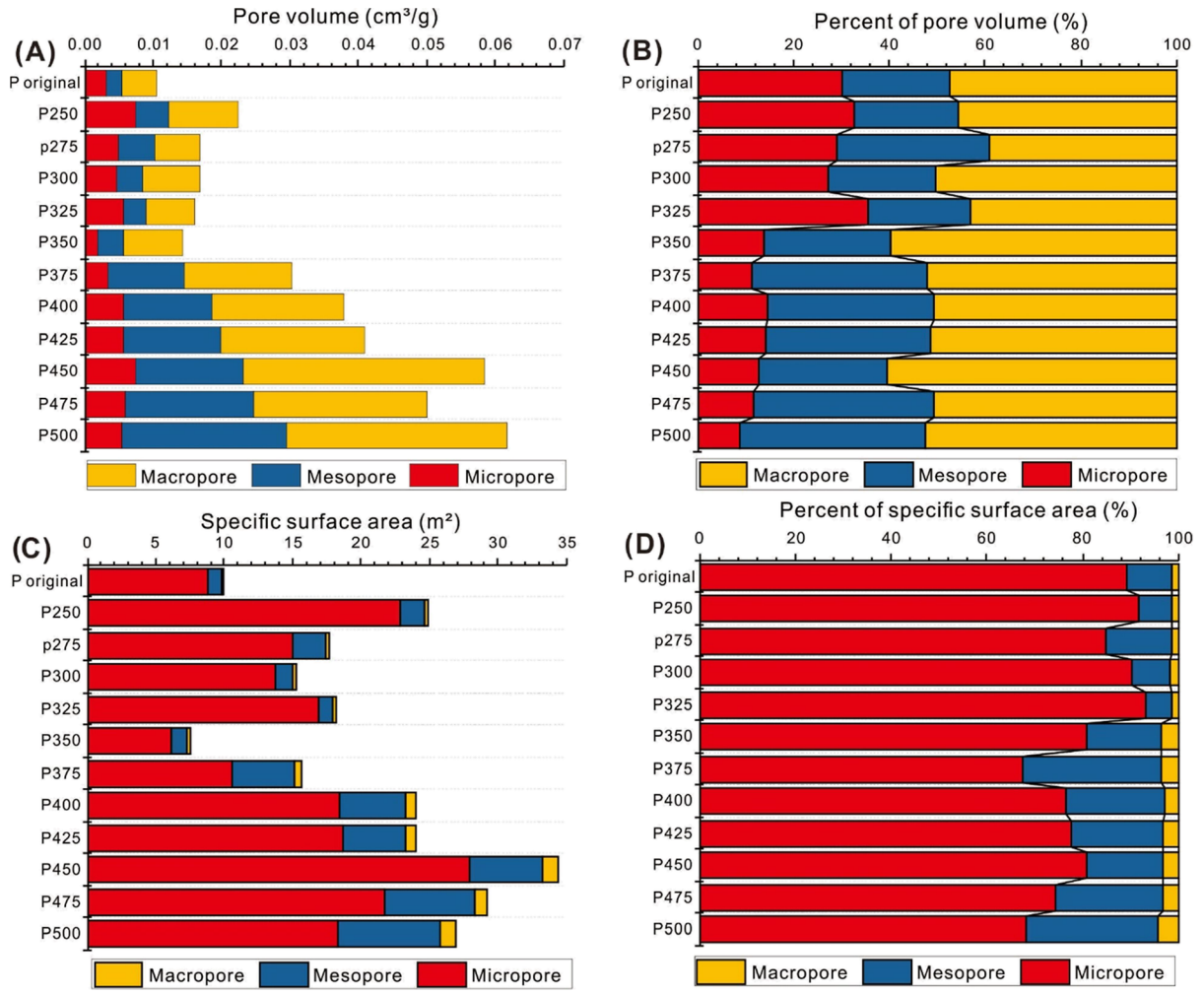

Figure 9. Volume and surface area of each type of pore, including macropores, mesopores, and micropores, both in absolute terms (A, C) and as a percentage (B, D) of P2d organic-rich shales. The PV is chiefly supplied by macropores, and the surface area is chiefly supplied by micropores.

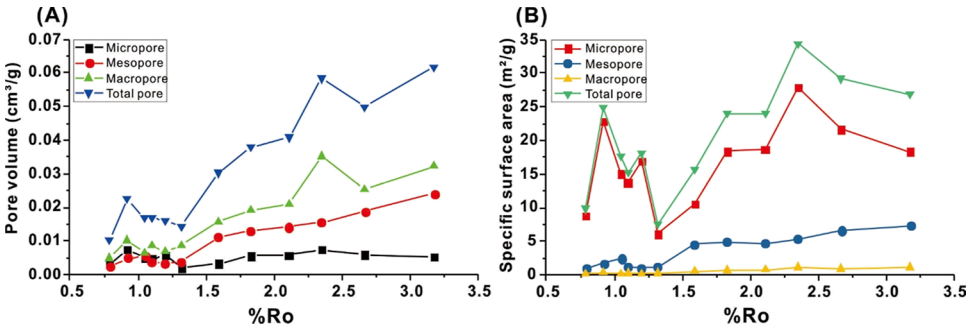

Figure 10. Development of (A) PV and (B) SSA with increased %R_o of P2d organic-rich shale. The total PV and SSA grow with increased thermal maturity. The lowest value of porosity occurs with the corresponding %R_o value of 1.32%. Two peaks in the PV and SSA are present, with the corresponding %R_o values of 0.92 and 2.35%, respectively.

evolution of the pore system in shale is still significantly influenced by thermal maturity. To illustrate the evolution of pore structure, the pore structure parameters including SSA and PV of marine shales were standardized to TOC content and associated with %R_o (Figure 13). The development of shale porosity may be more accurately described without the effect of TOC.

The evolution pathways of the surface area and PV have almost the same trend with increasing maturity. Every parameter of the pore structure, in particular, the micropore volume and micropore surface area in addition to SSA, display two distinct peaks with matching %R_o values in the ranges of 0.79−1.05 and 1.83−2.35%, respectively. These two peaks correspond to the best stage of pore development generated from kerogen, and the optimal periods of gas generation from the cracking of extractable OM.[57,79] When %R_o is between 1.1 and 1.83%, the volume and surface area of micropores decline, most likely as a result of extractable OM partially filling some micropores.[15]

As thermal maturity increases, the mesopore and macropore volume and surface area exhibit three peaks at %R_o values of

https://doi.org/10.1021/acs.energyfuels.3c00752
Energy Fuels XXXX, XXX, XXX−XXX

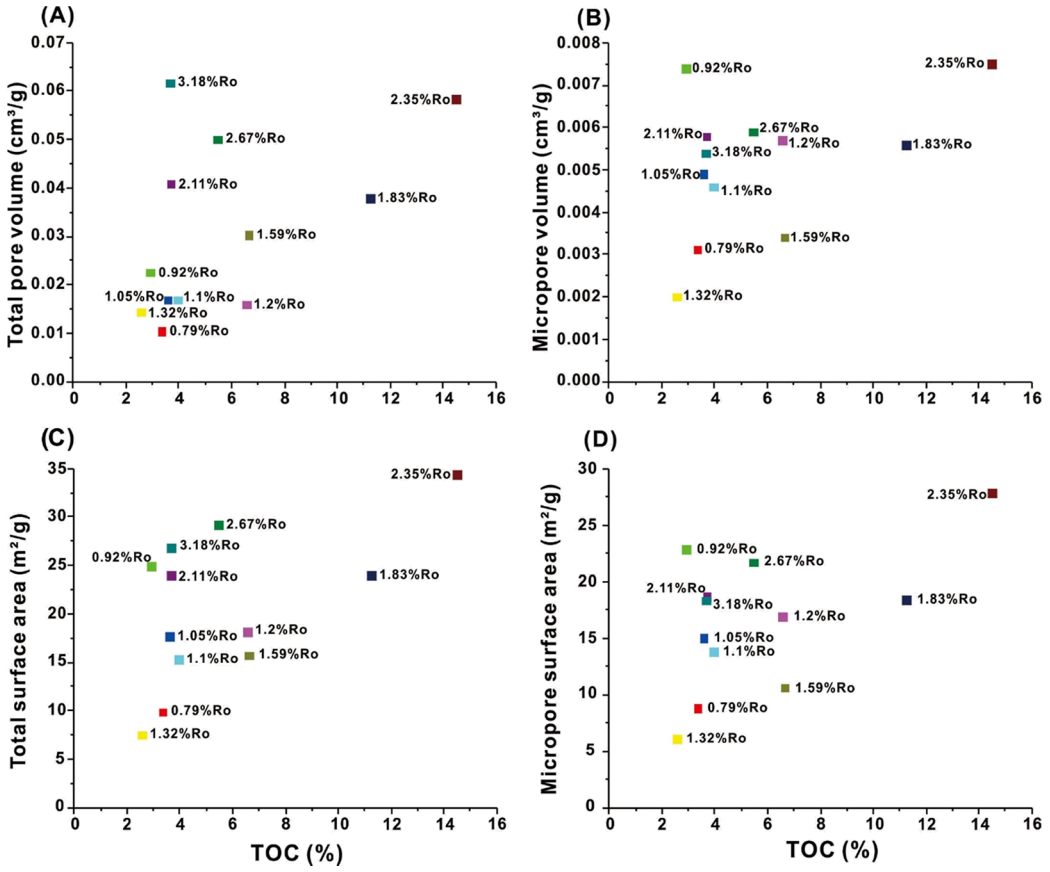

Figure 11. Associations between TOC content and (A) total PV, (B) micropore volume, (C) total surface area, and (D) micropore surface area for P2d organic-rich shale at different thermal simulation temperatures. The weak relation between TOC, SSA, and PV is probably due to the strong impact of thermal maturity that could reduce the effect of TOC impact; consequently, samples with higher maturity have higher porosity.

0.92, 1.32, and 2.11%, respectively. The increasing trend of the PV is attributed to pore development and generation. In contrast, the decreasing trend could be owing to oil-filling pores and cementation. As a result, the PV and SSA share two peaks; corresponding to $\%R_o$ values for peak I being in the range of 0.79 to 1.05% and peak II being in the range of 1.83 to 2.35% (Figure 13D,H). Peak I is associated with the last stages of oil generation and the latter stage of kerogen conversion to gas, while peak II is associated with the peak of gas generation created by the conversion of liquid hydrocarbons.[52,80,81] The PV of peak II is greater than that of peak I, showing that the best stage for porosity development is during the thermal conversion of oil to gas. This is mostly explained by the copious OM pores produced by oil cracking, which greatly increases the total PV.[57,82,83] Hence, the liquid hydrocarbon cracking into gas is the ideal stage for pore development. The second crucial stage for pore development is represented by the latter stage of kerogen cracking to gas. It is worthwhile to note that the evolution of shale pores was multistaged rather than increasing gradually.[36]

4.4. Porosity Evolution Model. Prior research studies have concentrated on the development of shale pores with increasing thermal maturity.[13,15,31,34,79,84] However, most of these research works ignore the process of pore evolution with maturity above 2.0%R_o. Topór et al.[57] illustrated the porosity development with $\%R_o$ between 0.4 and 3.5% for the Silurian shales from the Baltic basin. However, the lack of samples with $\%R_o$ > 2.0% raises questions regarding the pore evolution tendency. Figure 14 depicts a model of the full hydrocarbon generation process along with shale pore evolution based on a thorough examination of hydrocarbon formation and pore structure development with increasing thermal maturity. It is suggested that the porosity at the immature stage ($\%R_o$ < 0.5%) is higher than the porosity at the stage of early kerogen cracking.[15]

Between the late immature and early mature stages ($\%R_o$ = 0.3−0.7%), the PV decreases rapidly because of the impact of early compaction and cementation, whereas immature oil and early gas are the main generated hydrocarbons. During the mature stage with $\%R_o$ = 0.7−1.0%, a significant volume of oil and a negligible amount of related gas are generated. The total PV significantly increases, with a moderately clear growth trend in the macropore volume and a considerable increase in the micropore volume because of the hydrocarbon generation from kerogen cracking. Little organic pores are developed due to the maturation of kerogen owing to the production and expulsion of hydrocarbons within kerogen.[79,84] Clay mineral transformation and dissolution pores resulted from unstable minerals reacting with organic acid leading to a porosity increase. During the mature stage with $\%R_o$ = 1.0−1.2%, the PV shows a slightly decreasing trend because the generated liquid hydrocarbons cannot be expelled completely from the source rock and thus are filled within pore space.

The stage of maturity of $\%R_o$ = 1.1−1.6% represents the main stage of kerogen breaking into gas. The porosity significantly increases due to kerogen cracking into a gas.[15] The porosity decreases due to the cementation, especially with a $\%R_o$ of 1.6−1.83%. The porosity increased during the late stage of high maturity with $\%R_o$ = 1.83−2.1% as a result of the cracking of oil and kerogen to gas. A significant amount of organic pores are

https://doi.org/10.1021/acs.energyfuels.3c00752
Energy Fuels XXXX, XXX, XXX−XXX

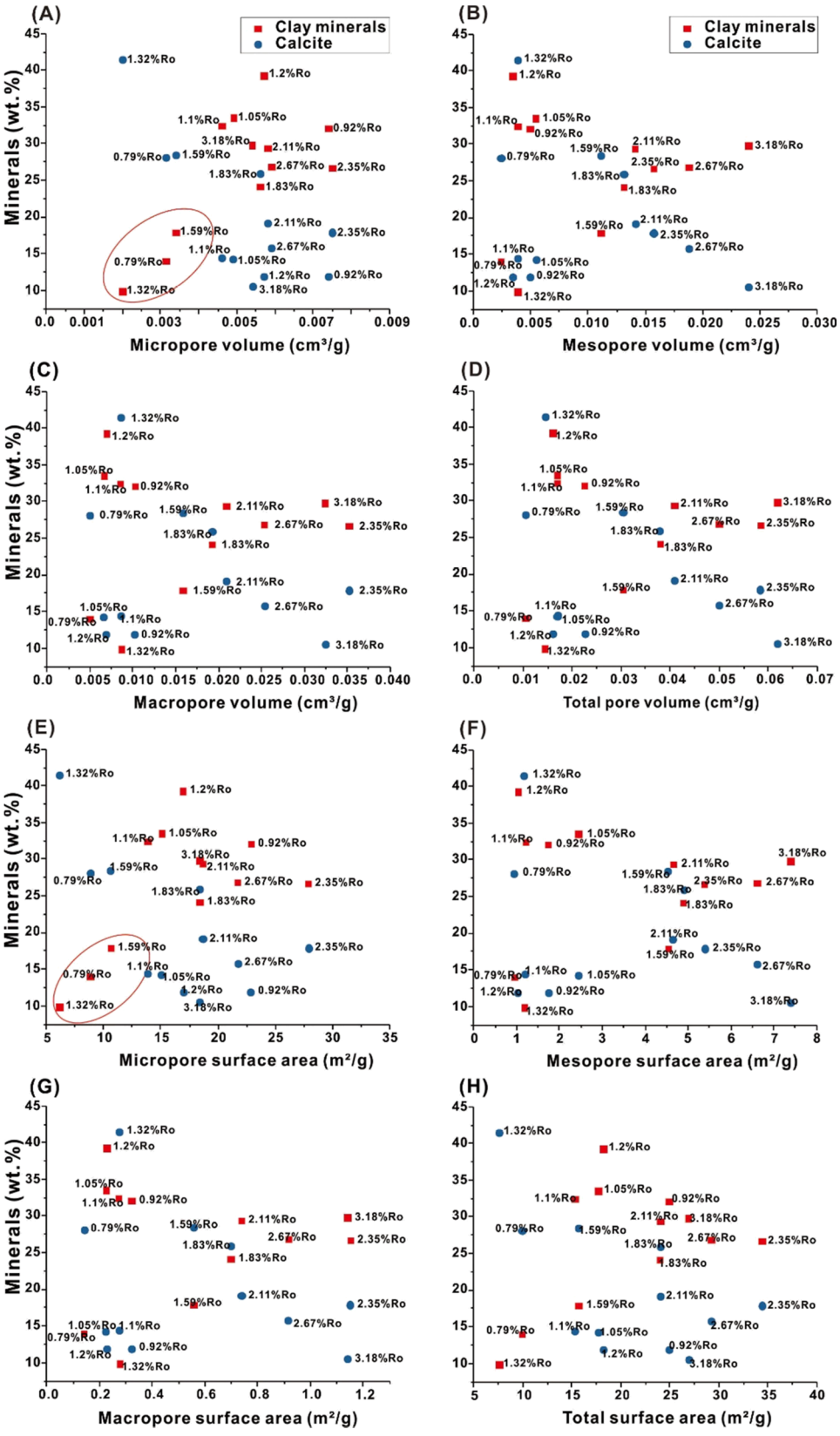

Figure 12. Relationships of pore structure including PV (A–D) and surface area (E–H) to clay minerals and calcite for P2d organic-rich shale at different thermal simulation temperatures. Calcite and clay minerals show a slight relationship with micropores and no clear connection was found with other pore structure characteristics. The micropore volume and surface area have favorable correlations with clay minerals and negative correlations with calcite (A, E).

created, which can compensate for the lack of pores brought on by metagenesis, causing the porosity to continuously increase. In the overmature stage, the PV progressively grows due to pore development resulting from dry gas generation from the

https://doi.org/10.1021/acs.energyfuels.3c00752
Energy Fuels XXXX, XXX, XXX−XXX

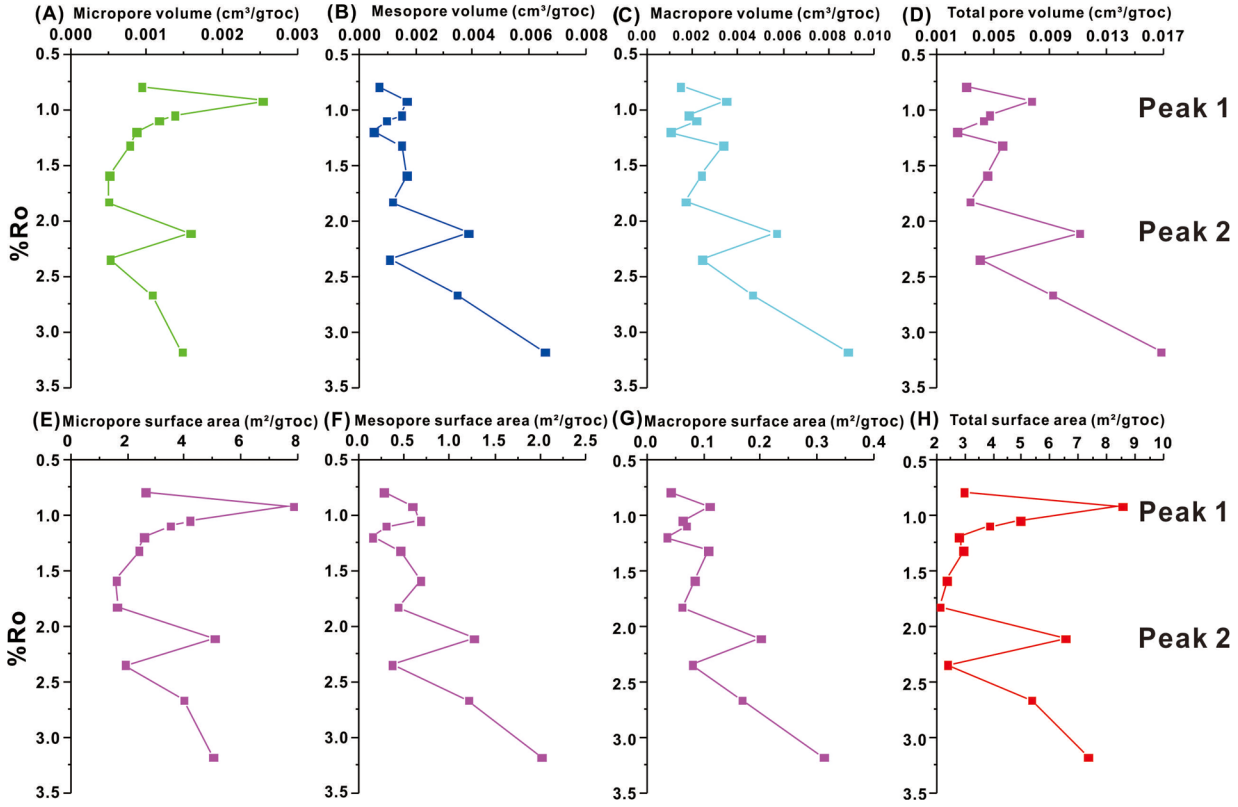

Figure 13. Evolution of the PV (A–D) and surface area (E–H) as thermal maturation increases. The pore parameters were normalized to TOC. The total PV and SSA increased with thermal maturity. The PV and SSA share two peaks with corresponding %R_o values of 0.92 and 2.35%, respectively. Peak I is associated with the last stages of oil production and the latter stage of kerogen conversion to gas, whereas peak II is related to the peak of gas generation created by the conversion of liquid hydrocarbons, which is the optimal pore formation period.

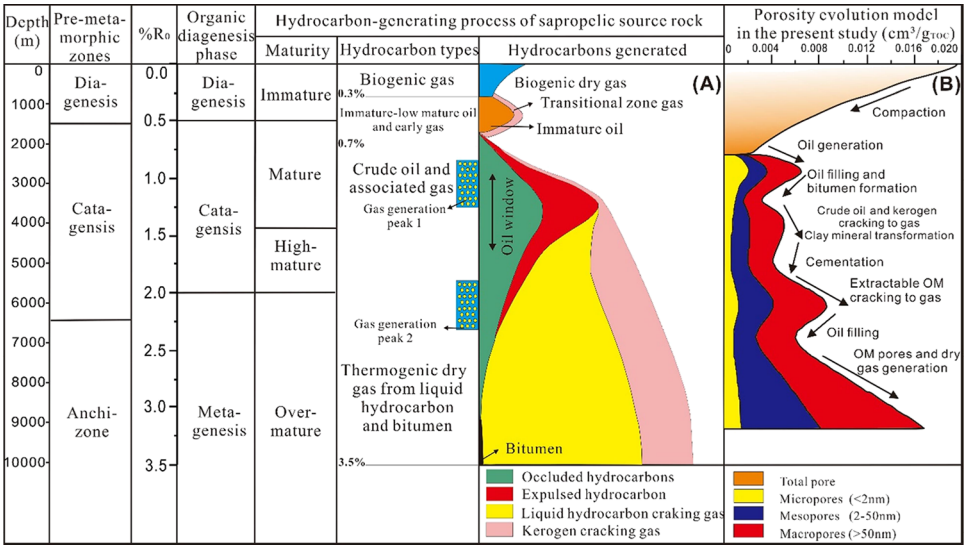

Figure 14. Schematic diagram of the porosity evolution of P2d organic-rich shale throughout the full hydrocarbon generation process; (A) hydrocarbon generation model (reproduced from Wang et al.[52] copyright 2019 American Chemical Society) and (B) porosity evolution model. In comparison to the original sample, pyrolysis samples have a higher porosity, which is associated with the development of organic pores throughout the conversion of kerogen to oil and bitumen. During the mature stage with %R_o = 1.0–1.2%, the porosity decreased due to the filling impact of oil formation. During the stage of maturity of %R_o = 1.1–1.6%, the occluded oil is cracking to gas and these filled pores are released leading to a porosity increase. Then, the porosity decreased owing to cementation. During the overmaturity stage %R_o > 2.0%, a large amount of dry gas was produced, and porosity increased continuously, while the micropores transformed into macropores.

occluded oil cracking. In the period of the highest gas generation rate (%R_o = 1.83–2.35%), the maximum peak of porosity occurs at a thermal maturity of 2.11 %R_o. A significant quantity of dry gas was generated by occluded oil or bitumen conversion during this period. Many OM pores were created during gas generation, greatly increasing the porosity of the shale. At the overmature

https://doi.org/10.1021/acs.energyfuels.3c00752
Energy Fuels XXXX, XXX, XXX–XXX

stage with a $\%R_o$ of 2.11−2.35%, the gas generation rate of residual oil or bitumen is low. As a result of oil filling, the macropores and total PV decrease. Cementation has a slight influence on porosity evolution during the overmaturity stage $\%R_o$ > 2.35%. The porosity shows an increasing trend with the highest PV at a $\%R_o$ of 3.18%, illustrating that the gas generation capacity of residual oil or bitumen is high, leading to the generation of abundant OM pores during the overmaturity stage.

5. CONCLUSIONS

1. With shale thermal maturation increasing, the parameters of oil and gas generation exhibit substantial differences. The crucial oil generation period of kerogen happens mostly when $\%R_o$ < 1.56%, with a maximum generation rate of 376.5 mg/g at $\%R_o$ of 1.38%. Thermal cracking from kerogen to gas occurs at $\%R_o$ ranging between 1.15 and 2.56%. When $\%R_o$ > 1.56%, the generated hydrocarbon gas content increases while the generated liquid hydrocarbon content decreases because residual oil starts to crack into gas. The major stage when immature oil cracks into gas occurs at a $\%R_o$ range between 1.56 and 3.45%.
2. Macropores are the primary source of PV for shales at various phases of thermal maturity, and mesopores and micropores come next. The SSA is offered by micropores, mesopores, and macropores, respectively. The overall PV and SSA increase with increasing thermal maturity. The PV and SSA share two common peaks with $\%R_o$ values of 0.92 and 2.35%, respectively. Peak I is associated with the last stages of oil generation and the latter stage of kerogen conversion to gas and peak II is associated with the cracking peak of liquid hydrocarbon to dry gas, which is the optimal pore formation period.
3. The porosity of P2d organic-rich shale is barely impacted by the TOC due to the main influence of maturity that can neutralize the influence of TOC. This means that the pores of shale increase significantly with thermal maturity, and the TOC content is a supporting factor because the numerous pores of OM were formed through the thermal cracking of liquid hydrocarbons to gas.
4. Porosity development is slightly influenced by mineralogical composition. Calcite content has a negative relationship with porosity due to the effect of maturation, while clay mineral has a positive relationship with porosity when $\%R_o$ < 1.59%. This indicates that clay mineral transformation has a moderate effect on pore structure at the low maturation to early oil window stage of P2d organic-rich shale.
5. Diagenesis and hydrocarbon generation processes are the main factors controlling shale pore formation and evolution. During the early diagenetic stage, porosity decreases due to cementation and filling by migrated organic materials. During the late diagenetic stage, the total PV increases dramatically due to the formation and development of OM pores created by the thermal cracking process of extractable OM and kerogen.

AUTHOR INFORMATION

Corresponding Author

Xiaowen Guo − *Key Laboratory of Tectonics and Petroleum Resources, Ministry of Education, China University of Geosciences, Wuhan 430074, China*; Phone: +86 15827499386; Email: guoxw@cug.edu.cn

Authors

Waheed Hammouri − *School of Earth Resources, China University of Geosciences, Wuhan 430074, China*; orcid.org/0000-0002-1197-4674

Mahmoud Abbas − *Institute of Marine Sciences, Guangdong Provincial Key Laboratory of Marine Disaster Prediction and Prevention, Shantou University, Shantou 515063, China*

Keqing Wang − *Key Laboratory of Tectonics and Petroleum Resources, Ministry of Education, China University of Geosciences, Wuhan 430074, China*

Complete contact information is available at: https://pubs.acs.org/10.1021/acs.energyfuels.3c00752

Author Contributions

W.H. conducted the investigation, methodology, software, formal analysis, and writing of the original draft. X.G. contributed to the conceptualization, writing—review and editing, resources, and supervision. M.A. contributed to writing—review and editing. K.W. contributed the methodology and data curation.

Notes

The authors declare no competing financial interest.

ACKNOWLEDGMENTS

The authors thank the editors and reviewers for the valuable comments that really improved the quality of the manuscript. We sincerely thank Mr. Zuo Gaokun and Jia Aoqi (China University of Geosciences, Wuhan) for their support in the lab and valuable discussion. The funding for this research was provided by the Chinese National Natural Science Foundation Joint Funds (No. U20B6001) and the Chinese National Natural Science Foundation (No. 41872139).

REFERENCES

(1) Curtis, J. B. Fractured Shale-Gas Systems. *AAPG Bull.* **2002**, *86*, 1921−1938.

(2) Chen, S.; Zhu, Y.; Wang, H.; Liu, H.; Wei, W.; Fang, J. Shale Gas Reservoir Characterisation: A Typical Case in the Southern Sichuan Basin of China. *Energy* **2011**, *36*, 6609−6616.

(3) Selley, R. C. UK Shale Gas: The Story so Far. *Mar. Pet. Geol.* **2012**, *31*, 100−109.

(4) Bai, B.; Elgmati, M.; Zhang, H.; Wei, M. Rock Characterization of Fayetteville Shale Gas Plays. *Fuel* **2013**, *105*, 645−652.

(5) Johnson, C.; Boersma, T. Energy (in) Security in Poland the Case of Shale Gas. *Energy Policy* **2013**, *53*, 389−399.

(6) Chalmers, G. R. L.; Bustin, R. M. The Organic Matter Distribution and Methane Capacity of the Lower Cretaceous Strata of Northeastern British Columbia, Canada. *Int. J. Coal Geol.* **2007**, *70*, 223−239.

(7) Clarkson, C. R.; Solano, N.; Bustin, R. M.; Bustin, A. M. M.; Chalmers, G. R. L.; He, L.; Melnichenko, Y. B.; Radliński, A. P.; Blach, T. P. Pore Structure Characterization of North American Shale Gas Reservoirs Using USANS/SANS, Gas Adsorption, and Mercury Intrusion. *Fuel* **2013**, *103*, 606−616.

(8) Cavelan, A.; Boussafir, M.; Rozenbaum, O.; Laggoun-Défarge, F. Organic Petrography and Pore Structure Characterization of Low-Mature and Gas-Mature Marine Organic-Rich Mudstones: Insights into Porosity Controls in Gas Shale Systems. *Mar. Pet. Geol.* **2019**, *103*, 331−350.

(9) Luo, P.; Zhong, N.; Khan, I.; Wang, X.; Wang, H.; Luo, Q.; Guo, Z. Effects of Pore Structure and Wettability on Methane Adsorption Capacity of Mud Rock: Insights from Mixture of Organic Matter and Clay Minerals. *Fuel* **2019**, *251*, 551−561.

(10) Ross, D. J. K.; Bustin, R. M. Shale Gas Potential of the Lower Jurassic Gordondale Member, Northeastern British Columbia, Canada. *Bull. Can. Pet. Geol.* **2007**, *55*, 51−75.
(11) Cao, T.; Deng, M.; Song, Z.; Luo, H.; Hursthouse, A. S. Characteristics and Controlling Factors of Pore Structure of the Permian Shale in Southern Anhui Province, East China. *J. Nat. Gas Sci. Eng.* **2018**, *60*, 228−245.
(12) Bustin, A. M. M.; Bustin, R. M.; Cui, X. Importance of Fabric on the Production of Gas Shales. In *SPE Unconventional Reservoirs Conference*; OnePetro, 2008; pp 114−167.
(13) Curtis, M. E.; Cardott, B. J.; Sondergeld, C. H.; Rai, C. S. Development of Organic Porosity in the Woodford Shale with Increasing Thermal Maturity. *Int. J. Coal Geol.* **2012**, *103*, 26−31.
(14) Loucks, R. G.; Reed, R. M.; Ruppel, S. C.; Hammes, U. Spectrum of Pore Types and Networks in Mudrocks and a Descriptive Classification for Matrix-Related Mudrock Pores. *AAPG Bull.* **2012**, *96*, 1071−1098.
(15) Mastalerz, M.; Schimmelmann, A.; Drobniak, A.; Chen, Y. Porosity of Devonian and Mississippian New Albany Shale across a Maturation Gradient: Insights from Organic Petrology, Gas Adsorption, and Mercury Intrusion. *AAPG Bull.* **2013**, *97*, 1621−1643.
(16) Löhr, S. C.; Baruch, E. T.; Hall, P. A.; Kennedy, M. J. Is Organic Pore Development in Gas Shales Influenced by the Primary Porosity and Structure of Thermally Immature Organic Matter? *Org. Geochem.* **2015**, *87*, 119−132.
(17) Sun, L.; Tuo, J.; Zhang, M.; Wu, C.; Wang, Z.; Zheng, Y. Formation and Development of the Pore Structure in Chang 7 Member Oil-Shale from Ordos Basin during Organic Matter Evolution Induced by Hydrous Pyrolysis. *Fuel* **2015**, *158*, 549−557.
(18) Ma, Z.; Zheng, L.; Xu, X.; Bao, F.; Yu, X. Thermal Simulation Experiment of Organic Matter-Rich Shale and Implication for Organic Pore Formation and Evolution. *Pet. Res.* **2017**, *2*, 347−354.
(19) Liu, B.; Schieber, J.; Mastalerz, M. Combined SEM and Reflected Light Petrography of Organic Matter in the New Albany Shale (Devonian-Mississippian) in the Illinois Basin: A Perspective on Organic Pore Development with Thermal Maturation. *Int. J. Coal Geol.* **2017**, *184*, 57−72.
(20) Chalmers, G. R.; Bustin, R. M.; Power, I. M. Characterization of Gas Shale Pore Systems by Porosimetry, Pycnometry, Surface Area, and Field Emission Scanning Electron Microscopy/Transmission Electron Microscopy Image Analyses: Examples from the Barnett, Woodford, Haynesville, Marcellus, and Doig Uni. *AAPG Bull.* **2012**, *96*, 1099−1119.
(21) Clarkson, C. R.; Wood, J. M.; Burgis, S. E.; Aquino, S. D.; Freeman, M. Nanopore-Structure Analysis and Permeability Predictions for a Tight Gas Siltstone Reservoir by Use of Low-Pressure Adsorption and Mercury-Intrusion Techniques. *SPE Reservoir Eval. Eng.* **2012**, *15*, 648−661.
(22) Liu, X.; Xiong, J.; Liang, L. Investigation of Pore Structure and Fractal Characteristics of Organic-Rich Yanchang Formation Shale in Central China by Nitrogen Adsorption/Desorption Analysis. *J. Nat. Gas Sci. Eng.* **2015**, *22*, 62−72.
(23) Xu, H.; Zhou, W.; Zhang, R.; Liu, S.; Zhou, Q. Characterizations of Pore, Mineral and Petrographic Properties of Marine Shale Using Multiple Techniques and Their Implications on Gas Storage Capability for Sichuan Longmaxi Gas Shale Field in China. *Fuel* **2019**, *241*, 360−371.
(24) Li, Y.; Yang, J.; Pan, Z.; Tong, W. Nanoscale Pore Structure and Mechanical Property Analysis of Coal: An Insight Combining AFM and SEM Images. *Fuel* **2020**, *260*, No. 116352.
(25) Cao, T.; Deng, M.; Cao, Q.; Huang, Y.; Yu, Y.; Cao, X. Pore Formation and Evolution of Organic-Rich Shale during the Entire Hydrocarbon Generation Process: Examination of Artificially and Naturally Matured Samples. *J. Nat. Gas Sci. Eng.* **2021**, *93*, 104020.
(26) Jarvie, D. M.; Hill, R. J.; Ruble, T. E.; Pollastro, R. M. Unconventional Shale-Gas Systems: The Mississippian Barnett Shale of North-Central Texas as One Model for Thermogenic Shale-Gas Assessment. *AAPG Bull.* **2007**, *91*, 475−499.
(27) Harwood, R. J. Oil and Gas Generation by Laboratory Pyrolysis of Kerogen. *AAPG Bull.* **1977**, *61*, 2082−2102.
(28) Lewan, M. D. Stable Carbon Isotopes of Amorphous Kerogens from Phanerozoic Sedimentary Rocks. *Geochim. Cosmochim. Acta* **1986**, *50*, 1583−1591.
(29) Song, D.; Tuo, J.; Wu, C.; Zhang, M.; Su, L. Comparison of Pore Evolution for a Mesoproterozoic Marine Shale and a Triassic Terrestrial Mudstone during Artificial Maturation Experiments. *J. Nat. Gas Sci. Eng.* **2020**, *75*, 103153.
(30) Javadpour, F.; Fisher, D.; Unsworth, M. Nanoscale Gas Flow in Shale Gas Sediments. *J. Can. Pet. Technol.* **2007**, *46*, 55−61.
(31) Guo, H.; Jia, W.; Zeng, J.; He, R. Evolution of Organic Matter and Nanometer-Scale Pores in an Artificially Matured Shale Undergoing Two Distinct Types of Pyrolysis: A Study of the Yanchang Shale with Type II Kerogen. *Org. Geochem.* **2017**, *105*, 56−66.
(32) Jiang, F.; Chen, J.; Xu, Z.; Wang, Z.; Hu, T.; Chen, D.; Li, Q.; Li, Y. Organic Matter Pore Characterization in Lacustrine Shales with Variable Maturity Using Nanometer-Scale Resolution X-Ray Computed Tomography. *Energy Fuels* **2017**, *31*, 2669−2680.
(33) Feiyu, W.; Jing, G.; Weiping, F.; Linyan, B. Evolution of Overmature Marine Shale Porosity and Implication to the Free Gas Volume. *Pet. Explor. Dev.* **2013**, *40*, 819−824.
(34) Fishman, N. S.; Hackley, P. C.; Lowers, H. A.; Hill, R. J.; Egenhoff, S. O.; Eberl, D. D.; Blum, A. E. The Nature of Porosity in Organic-Rich Mudstones of the Upper Jurassic Kimmeridge Clay Formation, North Sea, Offshore United Kingdom. *Int. J. Coal Geol.* **2012**, *103*, 32−50.
(35) Tang, X.; Zhang, J.; Jin, Z.; Xiong, J.; Lin, L.; Yu, Y.; Han, S. Experimental Investigation of Thermal Maturation on Shale Reservoir Properties from Hydrous Pyrolysis of Chang 7 Shale, Ordos Basin. *Mar. Pet. Geol.* **2015**, *64*, 165−172.
(36) Wu, S.; Yang, Z.; Zhai, X.; Cui, J.; Bai, L.; Pan, S.; Cui, J. An Experimental Study of Organic Matter, Minerals and Porosity Evolution in Shales within High-Temperature and High-Pressure Constraints. *Mar. Pet. Geol.* **2019**, *102*, 377−390.
(37) Liu, D.; Li, H.; Zhang, C.; Wang, Q.; Peng, P.'. Experimental Investigation of Pore Development of the Chang 7 Member Shale in the Ordos Basin under Semi-Closed High-Pressure Pyrolysis. *Mar. Pet. Geol.* **2019**, *99*, 17−26.
(38) Liang, C.; Jiang, Z.; Zhang, C.; Guo, L.; Yang, Y.; Li, J. The Shale Characteristics and Shale Gas Exploration Prospects of the Lower Silurian Longmaxi Shale, Sichuan Basin, South China. *J. Nat. Gas Sci. Eng.* **2014**, *21*, 636−648.
(39) Dong, D. Z.; Gao, S.; Huang, J. L.; Guan, Q.; Wang, S.; Wang, Y. A Discussion on the Shale Gas Exploration & Development Prospect in the Sichuan Basin. *Nat. Gas Ind.* **2014**, *34*, 1−15.
(40) Xia, M.; Wen, L.; Wang, Y.; Hong, H.; Fan, Y.; Wen, Y. High Quality Source Rocks in Trough Facies of Upper Permian Dalong Formation, Sichuan Basin. *Pet. Explor. Dev.* **2010**, *37*, 654−662.
(41) Wei, Z.; Wang, Y.; Wang, G.; Sun, Z.; Xu, L. Pore Characterization of Organic-Rich Late Permian Da-Long Formation Shale in the Sichuan Basin, Southwestern China. *Fuel* **2018**, *211*, 507−516.
(42) Wei, Z.; Wang, Y.; Wang, G.; Sun, Z.; Zhang, T.; Xu, L.; Ma, X.; He, W. Paleoenvironmental Conditions of Organic-Rich Upper Permian Dalong Formation Shale in the Sichuan Basin, Southwestern China. *Mar. Pet. Geol.* **2018**, *91*, 152−162.
(43) Song, D.; Tuo, J.; Zhang, M.; Wu, C.; Su, L.; Li, J.; Zhang, Y.; Zhang, D. Hydrocarbon Generation Potential and Evolution of Pore Characteristics of Mesoproterozoic Shales in North China: Results from Semi-Closed Pyrolysis Experiments. *J. Nat. Gas Sci. Eng.* **2019**, *62*, 171−183.
(44) Gao, Z.; Xiong, S. Methane Adsorption Capacity Reduction Process of Water-Bearing Shale Samples and Its Influencing Factors: One Example of Silurian Longmaxi Formation Shale from the Southern Sichuan Basin in China. *J. Earth Sci.* **2021**, *32*, 946−959.
(45) Li, Y.; Zhang, C.; Tang, D.; Gan, Q.; Niu, X.; Wang, K.; Shen, R. Coal Pore Size Distributions Controlled by the Coalification Process:

https://doi.org/10.1021/acs.energyfuels.3c00752
Energy Fuels XXXX, XXX, XXX−XXX

An Experimental Study of Coals from the Junggar, Ordos and Qinshui Basins in China. *Fuel* **2017**, *206*, 352−363.
(46) Brunauer, S.; Emmett, P. H.; Teller, E. Adsorption of Gases in Multimolecular Layers. *J. Am. Chem. Soc.* **1938**, *60*, 309−319.
(47) Barrett, E. P.; Joyner, L. G.; Halenda, P. P. The Determination of Pore Volume and Area Distributions in Porous Substances I. Computations from Nitrogen Isotherms. *J. Am. Chem. Soc.* **1951**, *73*, 373−380.
(48) Jia, A.; Hu, D.; He, S.; Guo, X.; Hou, Y.; Wang, T.; Yang, R. Variations of Pore Structure in Organic-Rich Shales with Different Lithofacies from the Jiangdong Block, Fuling Shale Gas Field, SW China: Insights into Gas Storage and Pore Evolution. *Energy Fuels* **2020**, *34*, 12457−12475.
(49) Cui, J. W.; Zhu, R. K.; Cui, J. G. Relationship of Porous Evolution and Residual Hydrocarbon: Evidence from Modeling Experiment with Geological Constrains. *Acta Geol. Sin.* **2013**, *87*, 730−736.
(50) Yang, R.; He, S.; Yi, J.; Hu, Q. Nano-Scale Pore Structure and Fractal Dimension of Organic-Rich Wufeng-Longmaxi Shale from Jiaoshiba Area, Sichuan Basin: Investigations Using FE-SEM, Gas Adsorption and Helium Pycnometry. *Mar. Pet. Geol.* **2016**, *70*, 27−45.
(51) Peng, N.; He, S.; Hu, Q.; Zhang, B.; He, X.; Zhai, G.; He, C.; Yang, R. Organic Nanopore Structure and Fractal Characteristics of Wufeng and Lower Member of Longmaxi Shales in Southeastern Sichuan, China. *Mar. Pet. Geol.* **2019**, *103*, 456−472.
(52) Wang, X.; Jiang, Z.; Jiang, S.; Chang, J.; Li, X.; Wang, X.; Zhu, L. Pore Evolution and Formation Mechanism of Organic-Rich Shales in the Whole Process of Hydrocarbon Generation: Study of Artificial and Natural Shale Samples. *Energy Fuels* **2019**, *34*, 332−347.
(53) Thommes, M.; Kaneko, K.; Neimark, A. V.; Olivier, J. P.; Rodriguez-Reinoso, F.; Rouquerol, J.; Sing, K. S. W. Physisorption of Gases, with Special Reference to the Evaluation of Surface Area and Pore Size Distribution (IUPAC Technical Report). *Pure Appl. Chem.* **2015**, *87*, 1051−1069.
(54) Bai, F.; Sun, Y.; Liu, Y.; Guo, M. Evaluation of the Porous Structure of Huadian Oil Shale during Pyrolysis Using Multiple Approaches. *Fuel* **2017**, *187*, 1−8.
(55) Zhao, J.; Jin, Z.; Jin, Z.; Hu, Q.; Hu, Z.; Du, W.; Yan, C.; Geng, Y. Mineral Types and Organic Matters of the Ordovician-Silurian Wufeng and Longmaxi Shale in the Sichuan Basin, China: Implications for Pore Systems, Diagenetic Pathways, and Reservoir Quality in Fine-Grained Sedimentary Rocks. *Mar. Pet. Geol.* **2017**, *86*, 655−674.
(56) Luan, G. Q.; Dong, C. M.; Ma, C. F.; Lin, C. Y.; Zhang, J. Y.; Lu, X. F. Pyrolysis Simulation Experiment Study on Diagenesis and Evolution of Organic-Rich Shale. *Acta Sedimentol. Sin.* **2016**, *34*, 1208−1216.
(57) Topór, T.; Derkowski, A.; Ziemiański, P.; Szczurowski, J.; McCarty, D. K. The Effect of Organic Matter Maturation and Porosity Evolution on Methane Storage Potential in the Baltic Basin (Poland) Shale-Gas Reservoir. *Int. J. Coal Geol.* **2017**, *180*, 46−56.
(58) Yang, C.; Zhang, J.; Tang, X.; Ding, J.; Zhao, Q.; Dang, W.; Chen, H.; Su, Y.; Li, B.; Lu, D. Comparative Study on Micro-Pore Structure of Marine, Terrestrial, and Transitional Shales in Key Areas, China. *Int. J. Coal Geol.* **2017**, *171*, 76−92.
(59) Li, Y.; Wang, Z.; Pan, Z.; Niu, X.; Yu, Y.; Meng, S. Pore Structure and Its Fractal Dimensions of Transitional Shale: A Cross-Section from East Margin of the Ordos Basin, China. *Fuel* **2019**, *241*, 417−431.
(60) Chen, L.; Jiang, Z.; Liu, Q.; Jiang, S.; Liu, K.; Tan, J.; Gao, F. Mechanism of Shale Gas Occurrence: Insights from Comparative Study on Pore Structures of Marine and Lacustrine Shales. *Mar. Pet. Geol.* **2019**, *104*, 200−216.
(61) Loucks, R. G.; Reed, R. M.; Ruppel, S. C.; Jarvie, D. M. Morphology, Genesis, and Distribution of Nanometer-Scale Pores in Siliceous Mudstones of the Mississippian Barnett Shale. *J. Sediment. Res.* **2009**, *79*, 848−861.
(62) Milliken, K. L.; Rudnicki, M.; Awwiller, D. N.; Zhang, T. Organic Matter−Hosted Pore System, Marcellus Formation (Devonian), Pennsylvania. *AAPG Bull.* **2013**, *97*, 177−200.
(63) Haynes, R. J.; Naidu, R. Influence of Lime, Fertilizer and Manure Applications on Soil Organic Matter Content and Soil Physical Conditions: A Review. *Nutr. Cycl. Agroecosyst.* **1998**, *51*, 123−137.
(64) Ross, D. J. K.; Bustin, R. M. The Importance of Shale Composition and Pore Structure upon Gas Storage Potential of Shale Gas Reservoirs. *Mar. Pet. Geol.* **2009**, *26*, 916−927.
(65) Kumar, V.; Sondergeld, C. H.; Rai, C. S. Nano to Macro Mechanical Characterization of Shale. In *SPE Annual Technical Conference and Exhibition*; OnePetro, 2012; pp 3421−3443.
(66) Modica, C. J.; Lapierre, S. G. Estimation of Kerogen Porosity in Source Rocks as a Function of Thermal Transformation: Example from the Mowry Shale in the Powder River Basin of WyomingEstimation of Kerogen Porosity as a Function of Thermal Transformation. *AAPG Bull.* **2012**, *96*, 87−108.
(67) Reed, R. M.; Loucks, R. G. Low-Thermal-Maturity (<0.7% VR) Mudrock Pore Systems: Mississippian Barnett Shale, Southern Fort Worth Basin. In *GCAGS*, 2015; pp 15−28.
(68) Xiong, J.; Liu, X.; Liang, L. Experimental Study on the Pore Structure Characteristics of the Upper Ordovician Wufeng Formation Shale in the Southwest Portion of the Sichuan Basin, China. *J. Nat. Gas Sci. Eng.* **2015**, *22*, 530−539.
(69) Bousige, C.; Ghimbeu, C. M.; Vix-Guterl, C.; Pomerantz, A. E.; Suleimenova, A.; Vaughan, G.; Garbarino, G.; Feygenson, M.; Wildgruber, C.; Ulm, F.-J.; Pellenq, R. J. M.; Coasne, B. Realistic Molecular Model of Kerogen's Nanostructure. *Nat. Mater.* **2016**, *15*, 576−582.
(70) Yang, F.; Ning, Z.; Liu, H. Fractal Characteristics of Shales from a Shale Gas Reservoir in the Sichuan Basin, China. *Fuel* **2014**, *115*, 378−384.
(71) Yang, F.; Ning, Z.; Wang, Q.; Liu, H. Pore Structure of Cambrian Shales from the Sichuan Basin in China and Implications to Gas Storage. *Mar. Pet. Geol.* **2016**, *70*, 14−26.
(72) Cao, Q.; Zhou, W.; Deng, H.; Chen, W. Classification and Controlling Factors of Organic Pores in Continental Shale Gas Reservoirs Based on Laboratory Experimental Results. *J. Nat. Gas Sci. Eng.* **2015**, *27*, 1381−1388.
(73) Ma, X.; Guo, S.; Shi, D.; Zhou, Z.; Liu, G. Investigation of Pore Structure and Fractal Characteristics of Marine-Continental Transitional Shales from Longtan Formation Using MICP, Gas Adsorption, and NMR (Guizhou, China). *Mar. Pet. Geol.* **2019**, *107*, 555−571.
(74) Chen, S.; Han, Y.; Fu, C.; Zhang, H.; Zhu, Y.; Zuo, Z. Micro and Nano-Size Pores of Clay Minerals in Shale Reservoirs: Implication for the Accumulation of Shale Gas. *Sediment. Geol.* **2016**, *342*, 180−190.
(75) Katsube, T. J.; Issler, D. R. Pore-Size Distributions of Shales from the Beaufort-Mackenzie Basin, Northern Canada. *Paper-Geological Survey of Canada* **1993**, 123.
(76) Chen; Xiao, X. Evolution of Nanoporosity in Organic-Rich Shales during Thermal Maturation. *Fuel* **2014**, *129*, 173−181.
(77) Kumar, A. Selly, Richard C. and Sonnenberg, Stephen A. 2015. Elements of Petroleum Geology. *Mar. Geod.* **2016**, *39*, 112−113.
(78) Songtao, W.; Rukai, Z.; Jinggang, C. U. I.; Jingwei, C.; Bin, B.; Zhang, X.; Xu, J.; Desheng, Z.; Jianchang, Y.; Xiaohong, L. Characteristics of Lacustrine Shale Porosity Evolution, Triassic Chang 7 Member, Ordos Basin, NW China. *Pet. Explor. Dev.* **2015**, *42*, 185−195.
(79) Cui, H.; Liang, F.; Ma, C.; Zhong, N.; Sha, Y.; Ma, W. Pore Evolution Characteristics of Chinese Marine Shale in the Thermal Simulation Experiment and the Enlightenment for Gas Shale Evaluation in South China. *Geosci. J.* **2019**, *23*, 595−602.
(80) Dai, H.; Shen, B.; Li, K.; Zhang, X.; Xu, X.; Xu, Z.; Zhou, J. Characteristics and Hydrocarbon-Generating Process of the Organic-Rich Shale of Permian Dalong Formation in North Sichuan: Pyrolysis Experiments with Geological Constrain. *J. Nanjing Univ. Nat. Sci.* **2020**, *56*, 382−392.
(81) Jiang, Z.; Yan, S.; Xianglu, T.; Zhuo, L. I.; Xingmeng, W.; Guozhen, W.; Zixin, X. U. E.; Xin, L. I.; Zhang, K.; Chang, J. Controlling Factors of Marine Shale Gas Differential Enrichment in Southern China. *Pet. Explor. Dev.* **2020**, *47*, 661−673.

https://doi.org/10.1021/acs.energyfuels.3c00752
Energy Fuels XXXX, XXX, XXX−XXX

(82) Han, Y.; Horsfield, B.; Wirth, R.; Mahlstedt, N.; Bernard, S. Oil Retention and Porosity Evolution in Organic-Rich Shales. *AAPG Bull.* **2017**, *101*, 807−827.
(83) Jian, L. I.; Wei, M. A.; Yifeng, W.; Dongliang, W.; Zengye, X. I. E.; Zhisheng, L. I.; Chenghua, M. A. Modeling of the Whole Hydrocarbon-Generating Process of Sapropelic Source Rock. *Pet. Explor. Dev.* **2018**, *45*, 461−471.
(84) Ko, L. T.; Ruppel, S. C.; Loucks, R. G.; Hackley, P. C.; Zhang, T.; Shao, D. Pore-Types and Pore-Network Evolution in Upper Devonian-Lower Mississippian Woodford and Mississippian Barnett Mudstones: Insights from Laboratory Thermal Maturation and Organic Petrology. *Int. J. Coal Geol.* **2018**, *190*, 3−28.

https://doi.org/10.1021/acs.energyfuels.3c00752
Energy Fuels XXXX, XXX, XXX−XXX